



The soft impact of composite sandwich beams with a square-honeycomb core

B.P. Russell, T. Liu, N.A. Fleck, V.S. Deshpande*

Department of Engineering, University of Cambridge, Trumpington Street, Cambridge CB2 1PZ, UK

ARTICLE INFO

Article history:

Received 25 June 2010

Received in revised form

22 April 2011

Accepted 26 April 2011

Available online 18 May 2011

Keywords:

Composite lattice cores

Impact testing

Dynamic loads

Material rate-dependence

ABSTRACT

The dynamic response of end-clamped monolithic beams and sandwich beams of equal areal mass have been measured by loading the beams at mid-span with metal foam projectiles to simulate localised blast loading. The sandwich beams were made from carbon fibre laminate and comprised identical face sheets and a square-honeycomb core. The transient deflection of the beams was determined as a function of projectile momentum, and the measured response was compared with finite element simulations based upon a damage mechanics approach. A range of failure modes were observed in the sandwich beams including core fracture, plug-type shear failure of the core, debonding of the face sheets from the core and tensile tearing of the face sheets at the supports. In contrast, the monolithic beams failed by a combination of delamination of the plies and tensile failure at the supports. The finite element simulations of the beam response were accurate provided the carbon fibre properties were endowed with rate sensitivity of damage growth. The relative performance of monolithic and sandwich beams were quantified by the maximum transverse deflection at mid-span for a given projectile momentum. It was found that the sandwich beams outperformed both monolithic composite beams and steel sandwich beams with a square-honeycomb core. However, the composite beams failed catastrophically at a lower projectile impulse than the steel beams due to the lower ductility of the composite material.

© 2011 Elsevier Ltd. All rights reserved.

1. Introduction

Sandwich beams with composite face sheets and a lightweight foam core are commonly used in lightweight structures. Thus, it is important to measure and predict their deformation and fracture behaviours under both static and dynamic loadings. A literature has now been established for the measured and predicted properties of composite sandwich structures under static loading. For example, Steeves and Fleck [1] have investigated the static three-point bending response of simply supported sandwich beams made from glass-epoxy face sheets and a polymer foam core. Subsequently, Tagarielli et al. [2] investigated the effect of fully clamped boundary conditions upon the static bending response of these beams. The main modes of deformation and failure under static loading are reviewed in the books of Zenkert [3], Gibson and Ashby [4] and Ashby et al. [5] while Abrate [6] has summarised the failure of composite structures under low velocity impact.

The behaviour of composite sandwich structures subjected to low speed impact is broadly understood. In the aerospace industry, the focus of attention has been mainly upon barely visible impact

damage due to low speed impact. For example, dropping a wrench upon a composite structure induces delamination and leads to a reduction of compressive strength, see for example Olsson et al. [7] and the detailed delamination studies of Xu and Rosakis [8,9]. Likewise, in the automotive industry, the concern is with relatively low impact speeds (on the order of 10–30 m s⁻¹). Herup and Palazotto [10] have studied the low velocity impact response of sandwich structures with a composite skin and Nomex honeycomb. Mines et al. [11], Abrate [12] and Olsson [13] have determined the severity of impact to induce upper skin failure, core crush, lower skin failure and the perforation of sandwich panels containing aluminium or Nomex honeycomb cores. These studies have also elucidated the relationship between failure mechanism and the force versus time trace.

Comparatively little is known about the resistance of composite sandwich structures to intense, distributed dynamic loads. Olsson et al. [13] and Moyer et al. [14] performed finite element (FE) calculations to investigate the shock response of glass fibre reinforced polymer (GFRP) sandwich structures absent the effects of fluid–structure interaction. Mäkinen [15] extended these numerical studies to underwater shock loading in a one-dimensional setting and demonstrated that the acoustic mismatch between the water and composite face-sheets enhances the fluid–structure interaction effect, thereby increasing the resistance of composite

* Corresponding author. Tel.: +44 1223 332664.

E-mail address: vsd@eng.cam.ac.uk (V.S. Deshpande).

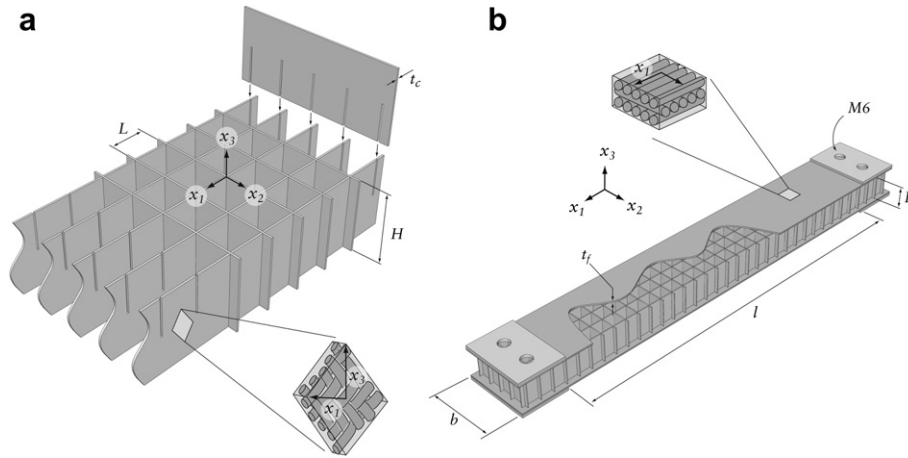


Fig. 1. Sketches of (a) the slotting used to assemble the square-honeycomb sandwich cores and the (b) assembled sandwich beams. The co-ordinate system associated with the core and beam as well as the notation used to indicate the dimensions of the honeycomb core and sandwich beam are included in the figure.

sandwich beams to underwater shock loading. Experimental investigations on military applications of composite structures have focused mainly on their perforation resistance to sharp projectiles, see for example the monograph by Abrate [12].

Little data exist in the open literature on the intense shock loading of composite sandwich structures. Tagarielli et al. [16] have investigated the shock response of sandwich beams with GFRP face sheets and PVC foam cores using the metal foam impact technique of Radford et al. [17]: impact of the structure by a metal foam projectile generates pressure pulses on the order of 100 MPa and loading times of approximately 0.1 ms. Using this technique, Tagarielli et al. [16] have shown that composite sandwich beams outperform their monolithic counterparts. (Likewise, Radford et al. [18] and Rathbun et al. [19] have demonstrated that metallic sandwich beams with lattice cores have higher dynamic strengths than metallic monolithic beams.)

Recently, Russell et al. [20] have investigated the quasi-static performance of carbon fibre composite sandwich beams with a square-honeycomb core. They found that the Matzenmiller et al. [21] and Hashin [22] damage model accurately captures the load versus displacement response, and predicts the active failure modes, for a range of beam geometries under both clamped and simply supported conditions. In the current study rate sensitivity must be added to the damage models in order to obtain satisfactory agreement with the observed dynamic response of end-clamped composite beams. The aims of the study are:

- Investigate the dynamic failure modes of shock-loaded carbon fibre sandwich beams with square-honeycomb cores.
- Compare the dynamic performance of the composite sandwich beams to their monolithic counterparts and to competing metallic concepts.
- Determine the fidelity of the Matzenmiller et al. [21] and Hashin [21] damage-mechanics models in predicting the observed dynamic responses and failure modes via 3D finite element calculations.

2. Experimental investigation

2.1. Materials

The square-honeycomb cores were manufactured by slotting together woven carbon fibre composite sheets of thickness $t_c = 0.35$ mm and density $\rho = 1370$ kg/m³. The composite sheets

comprised Toray T300-6k fibres (diameter 7 μ m) and Fiberite 934 epoxy arranged in a 2 \times 2 twill weave architecture with 3.7 tows per centimetre. The face sheets of the sandwich beams each comprised a [0/90/0] laminate of IM7-12k carbon fibres/HexPly[®] 8552 resin pre-preg. Each ply of the laminate was of thickness 0.25 mm thick and density $\rho = 1570$ kg/m⁻³. A [0/90/0] lay-up was chosen for the face sheets as such a laminate is easier to clamp via bolting compared to a unidirectional laminate that tends to split around the bolt holes.

2.2. Manufacture

The square-honeycomb cores were manufactured using the method devised by Russell et al. [23], summarised as follows. The 0.35 mm thick woven composite sheets were cut into rectangles of height $H = 14.2$ mm such that the fibre tows were at $\pm 45^\circ$ with respect to the height-direction, that is to the x_3 -axis (Fig. 1). Slots of height 7.1 mm, width $\Delta t_c = 45$ μ m and spaced at $L = 7.1$ mm were cut into the woven composite sheets using a 2-axis milling machine. The slotted sheets were then assembled to form a square-honeycomb of length 250 mm, width 35 mm and relative density $\bar{\rho} = 0.1$, as shown in Fig. 1a. After assembly, a low-viscosity epoxy adhesive (Opti-tec 5001¹) was applied to the joints of the core and was cured for 1 h at 65 $^\circ$ C.

Each face of the sandwich beams was of overall thickness $t_f = 0.75$ mm and of lay-up [0/90/0]: a 90 $^\circ$ mid-layer was sandwiched between two 0 $^\circ$ layers, such that the 0 $^\circ$ direction was aligned with the length of the beam, as sketched in Fig. 1. These faces were of length 250 mm and width 35 mm, and were cut from cured laminated sheets using a diamond saw. The faces were then bonded to the square-honeycomb core via a nylon-backed film epoxy (Redux 319² with an areal density of 0.40 kg m⁻²): this epoxy film was placed on one side of each of the face sheets and the sandwich assembly, comprising face sheets and core, was oven-cured at 175 $^\circ$ C for 1 h.

Some additional steps were taken to ensure that the beams could be adequately end-clamped. The clamping fixture is sketched in Fig. 2 and was used to clamp the end portions of the beams over a 25 mm length, thereby minimising rotation and minimising deflections of the beam ends in the transverse and longitudinal

¹ Intertronics, 17 Station Field Industrial Estate, Banbury Road, Kidlington, Oxfordshire OX5 1JD, UK.

² Hexcel Composites, Duxford, UK.

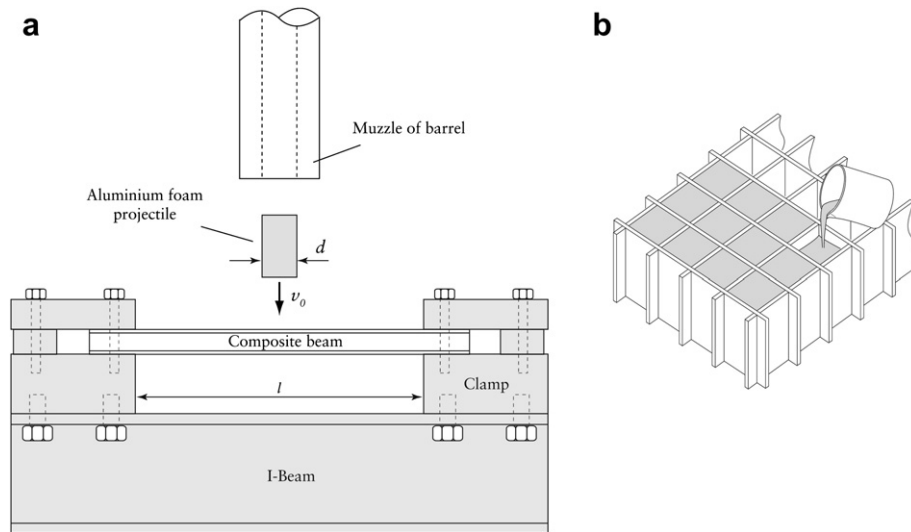


Fig. 2. Sketches of (a) the clamping fixture for the sandwich beams and (b) the sandwich beams with end portions filled with epoxy so as to allow high clamping pressures to be applied.

directions. The honeycomb cores of the sandwich beams were filled with an epoxy resin (Biresin[®] G30³) over the 25 mm clamped portion (3 rows of cells), and aluminium tabs were adhered to the face sheets. A high clamping pressure could then be applied to the sandwich beam via M6 bolts (Fig. 2). A sketch of the sandwich beam and its leading dimensions is included in Fig. 1. The clamped beams had a free span of $l = 200$ mm, and the areal density of the composite beams was $M = 5.89 \text{ kg m}^{-2}$.

Monolithic beams of areal mass equal to that of the sandwich beams were fabricated from the IM7-8552 pre-preg. In order to attain the same areal mass as the sandwich beams, 15 plies were laid-up with alternating 0° and 90° fibre orientations, as denoted by $[(0/90)_3/0/90]^s$. The monolithic beams, of thickness $t = 3.75$ mm, were cut to a length of 250 mm and width of 35 mm (i.e. identical to that of the sandwich beams). Aluminium tabs of length 25 mm were glued to the two ends and the beams were end-clamped as described above.

2.3. Mechanical properties of the composites sheets

The quasi-static uniaxial compressive and tensile responses were measured for the face sheet and core materials at an applied nominal strain rate 10^{-3} s^{-1} using the procedure as detailed by Russell et al. [23]. In brief, dog-bone shaped specimens were cut from $[0/90]$ and $[45/-45]$ laminates. The tensile responses were measured using a screw-driven test machine, with friction gripping of the specimens. The applied load was measured via the load cell of the test machine and was used to define the applied stress while a $0-90^\circ$ strain gauge rosette was used to measure the axial and transverse components of strain. In order to prevent Euler buckling of the specimens during the compression tests, a sandwich column was constructed comprising face sheets of the composite material and an aluminium hexagonal honeycomb core of relative density 2.5% and thickness 10 mm. Otherwise, the test procedure for the compression tests was the same as that for the tensile tests.

The measured tensile and compressive responses of the laminates are plotted in Fig. 3a and b, respectively, for the $[0/90]$ and $[45/-45]$ laminates. Both orientations display an elastic-brittle response in tension and in compression. The modulus of the of $[0/90]$ laminate is $E_l^0 = 85 \text{ GPa}$ while its compressive and tensile strengths are

$\sigma_l^{0c} = 630 \text{ MPa}$ and $\sigma_l^{0t} = 980 \text{ MPa}$, respectively. The corresponding properties of the woven material are $E_w^0 = 63 \text{ GPa}$, $\sigma_w^{0c} = 330 \text{ MPa}$ and $\sigma_w^{0t} = 540 \text{ MPa}$. In contrast, the response of both the laminated and woven materials in the $\pm 45^\circ$ orientation is dominated by shear of the matrix; hence, this orientation is weaker but more ductile than the $[0/90]$ orientation, in both tension and compression. The (unloading) modulus of the laminate is $E_l^{45} = 16 \text{ GPa}$ while the tensile and compressive strengths are $\sigma_l^{45t} = 115 \text{ MPa}$ and $\sigma_l^{45c} = 215 \text{ MPa}$, respectively. The corresponding properties of the woven material are $E_w^{45} = 16 \text{ GPa}$, $\sigma_w^{45t} = 175 \text{ MPa}$ and $\sigma_w^{45c} = 190 \text{ MPa}$. These values are used subsequently in the finite element calculations.

2.4. Protocol for the dynamic tests

Alporas aluminium foam projectiles were used to provide impact loading of the clamped monolithic and sandwich beams over a central circular patch, as shown in Fig. 2. The use of foam projectiles as a means of providing well-characterised pressure versus time has recently been developed by Radford et al. [17] and subsequently employed to investigate the dynamic response of sandwich beams with lattice cores (Radford et al. [18]), and of circular sandwich plates with metal foam cores (Radford et al. [24]) and lattice cores (McShane et al. [25]).

Circular cylindrical projectiles of length $l_0 = 50$ mm and diameter $d = 28.5$ mm were electro-discharge machined from Alporas foam blocks of density $\rho_p = 300 \text{ kg m}^{-3}$. The projectiles were fired from a gas gun of bore diameter 28.6 mm and length 4.5 m, at a velocity v_0 in the range 156 m s^{-1} to 340 m s^{-1} , providing a projectile momentum per unit area $I_0 = \rho_p l_0 v_0$ of up to 3.2 kN s m^{-2} . High-speed photography was used to observe the dynamic transverse deformation of the beams. An Itronx DRS ultra-8 camera was used with an inter-frame time of 67 μs and an exposure time of 5 μs .

3. Experimental results

3.1. The sandwich beams

Six levels of initial momentum were applied to both the monolithic and sandwich beams, and the deformation and failure mechanisms were observed. Montages showing the sequence of deformation of the sandwich beams subjected to three impulse levels,

³ Sika, Watchmead, Welwyn Garden City, Hertfordshire AL7 1BQ, UK.

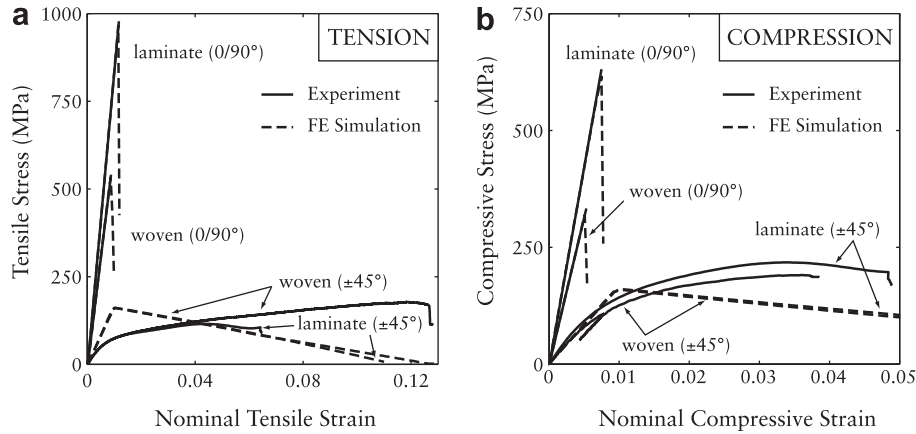


Fig. 3. The measured tensile and compressive quasi-static stress versus strain responses of the (a) laminate composite (comprising two orthogonal unidirectional plies) and (b) the woven composite materials. The responses are shown for both the 0° – 90° and $\pm 45^\circ$ orientations. The corresponding predictions of the calibrated constitutive model are included in the figure.

$I_0 = 1.83$ kPa s, 2.73 kPa s and 3.16 kPa s, are included in Fig. 4; the time $t = 0$ corresponds to the instant that the metal foam projectile impacts the beams. The measured deflection of the back face at mid-span are taken from the high speed images and are plotted as a function of time t in Fig. 5 for all six impulse levels investigated here. At $I_0 = 1.83$ kPa s, the beam response is essentially elastic with negligible permanent deformation. At the intermediate impulse of 2.73 kPa s, larger deflections are observed and some permanent deformation occurs. The deformation of the beam subjected of the 3.16 kPa s impulse shows a distinct change of mode. Deformation localises near the impact site ($t = 1.29$ μ s) followed by a plug-type shear failure at the edge of the impact site ($t = 299$ μ s). The shear failure of the core initiates debonding of the back face sheet from the core.

Deformation of the composite sandwich beam is primarily elastic in nature: high-speed elastic flexural waves cause deformation to be spread across the entire span of the beam early in the deformation history: flexural wave propagation along the beam length is sufficiently rapid for it not be observed in the images taken at the inter-frame time of 67 μ s.

The resolution of the images taken during high speed photography is not sufficient to visualise details of the failure processes at the lower impulses (i.e. $I_0 < 3.0$ kPa s). These failure modes are best observed by a post-test inspection of the beams. Four regimes of behaviour were inferred from these observations:

- At impulses below 1.8 kPa s, no visible damage/failure of the beams was observed suggesting that the response of the beams was purely elastic.
- Over the impulse range 1.8 kPa s $< I_0 < 2.86$ kPa s fracture of the core was observed at mid-depth of the beam, as shown in Fig. 6a.
- At impulses 2.87 kPa s $< I_0 < 3.15$ kPa s, a plug-type shear failure was observed in the core at the edges of the impact site. Associated with this shear failure is debonding of the back face sheet from the core, as illustrated in the sketches and photographs of Fig. 6b.
- Debonding of the back face leads to failure of the back face near the supports at impulses $I_0 \geq 3.15$ kPa s, see Fig. 6c.

3.2. The monolithic beams

The observed sequence of deformation of the monolithic beams subjected to three impulse levels is shown in Fig. 7; these impulses are approximately equal to the values imposed on the sandwich beams as reported in Fig. 4. Additionally, the corresponding measured deflections at mid-span as a function of time t are

included in Fig. 8 for all six impulse levels investigated here. The lower flexural rigidity of the monolithic beams compared to the sandwich beams results in lower flexural wave speeds in the monolithic beams. Consequently, the inter-frame time is sufficiently short for a flexural wave, emanating from the impact site and travelling towards the supports, to be visible in the high speed images. Delamination of the plies is observed in the high speed images for $I_0 = 3.18$ kPa s but no other failure modes were visible in the high speed images. Post-test inspection of the monolithic beams revealed the following regimes of behaviour:

- No visible damage and no permanent deformation for impulses $I_0 < 1.7$ kPa s.
- Delamination initiated near the supports at impulses around $I_0 < 2.7$ kPa s.
- Over the impulse range 2.7 kPa s $\leq I_0 < 3.18$ kPa s delaminations extended over the entire span of the beam.
- At impulses $I_0 \geq 3.18$ kPa s, complete failure of the beam occurred by a combination of fibre fracture and multiple delaminations.

Photographs of selected as-tested monolithic beams are included in Fig. 9 to illustrate these failure modes.

4. Finite element calculations

We now report finite element (FE) calculations of the impact response of the composite square-honeycomb core sandwich beams. The main aims of these calculations are to:

- Investigate the ability of the Matzenmiller et al. [21] and Hashin [22] constitutive model for fibre composites, as implemented in the commercial finite element code ABAQUS, to capture the observed deformation and failure modes.
- Investigate the role of material rate sensitivity and delamination on the dynamic deformation and damage modes of the composite monolithic and sandwich beams.

We emphasize here that the composite model employed here was not specifically developed for the problem under consideration here and may have some parameters that are superfluous in terms of the problem at hand. However, it is the aim of this study to investigate the fidelity of the Matzenmiller et al. [21] and Hashin [22] constitutive model for a complex structure and hence we do not attempt to modify/simplify this model for current purposes.

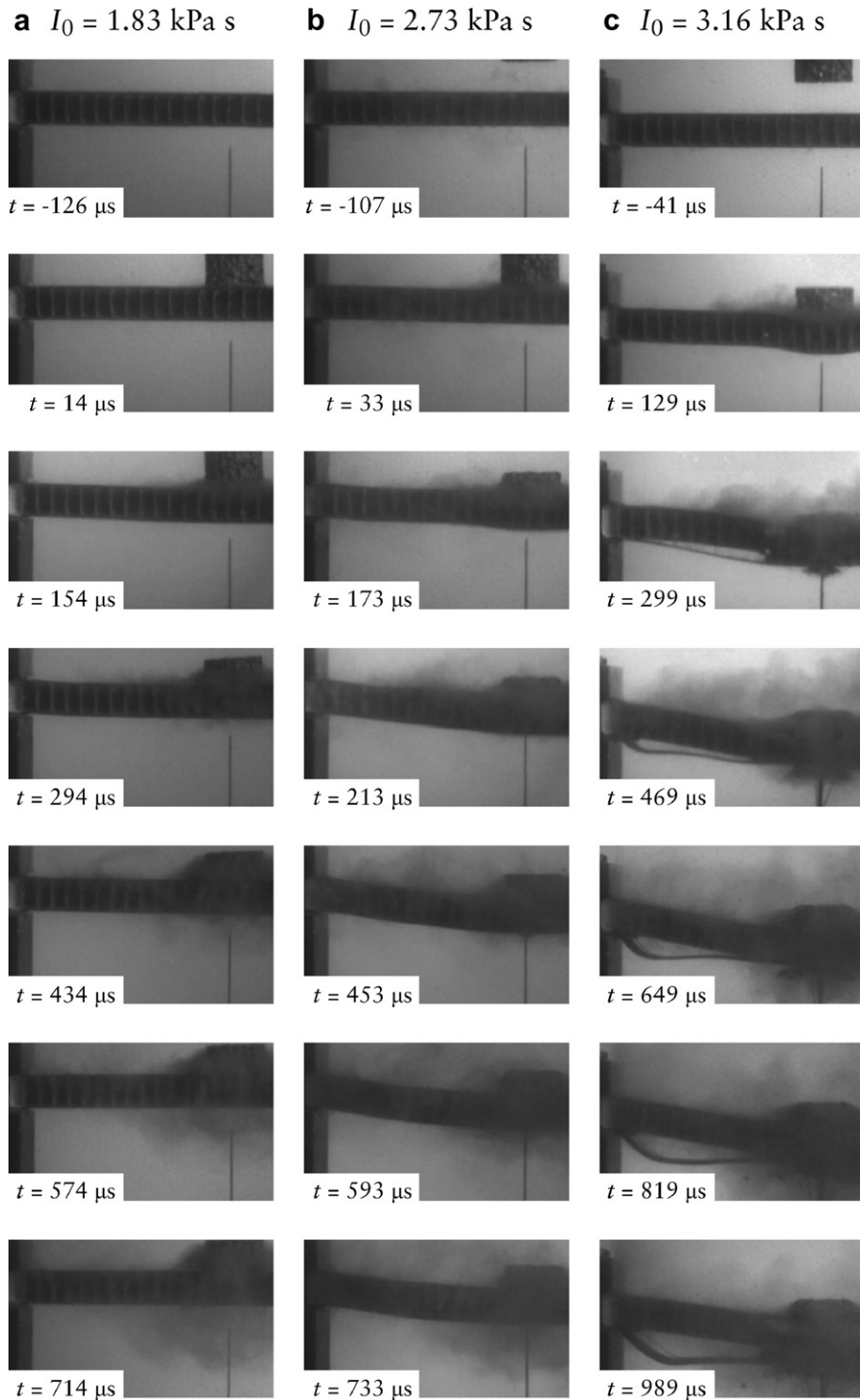


Fig. 4. Montage of high speed images showing the observed sequence of deformation of the sandwich beams subjected to three levels of impulse I_0 (a) 1.83 kPa s, (b) 2.73 kPa s and (c) 3.16 kPa s via the metal foam impact. Time $t = 0$ corresponds to the instant that the metal foam projectile impacts the beam.

4.1. Description of FE model

Finite strain, three dimensional (3D) FE simulations were conducted using the explicit version of the commercial finite element package ABAQUS (version 6.8). Dynamic loading of each plate was simulated by the impact of a foam projectile: at the start of the simulation, the projectile was imparted with a uniform initial velocity v_0 and was brought into contact with the plate at its

mid-span. The cylindrical foam projectiles of diameter 28.5 mm and length 50 mm were modelled using linear hexahedral and wedge elements (C3D8R and C3D6, respectively in ABAQUS notation) with the elements swept about the cylindrical axis of the foam projectile.

The “general contact” option in ABAQUS was employed to simulate contact between all possible surfaces: the core and the face sheets, self-contact of the core, contact of the two face sheets, and

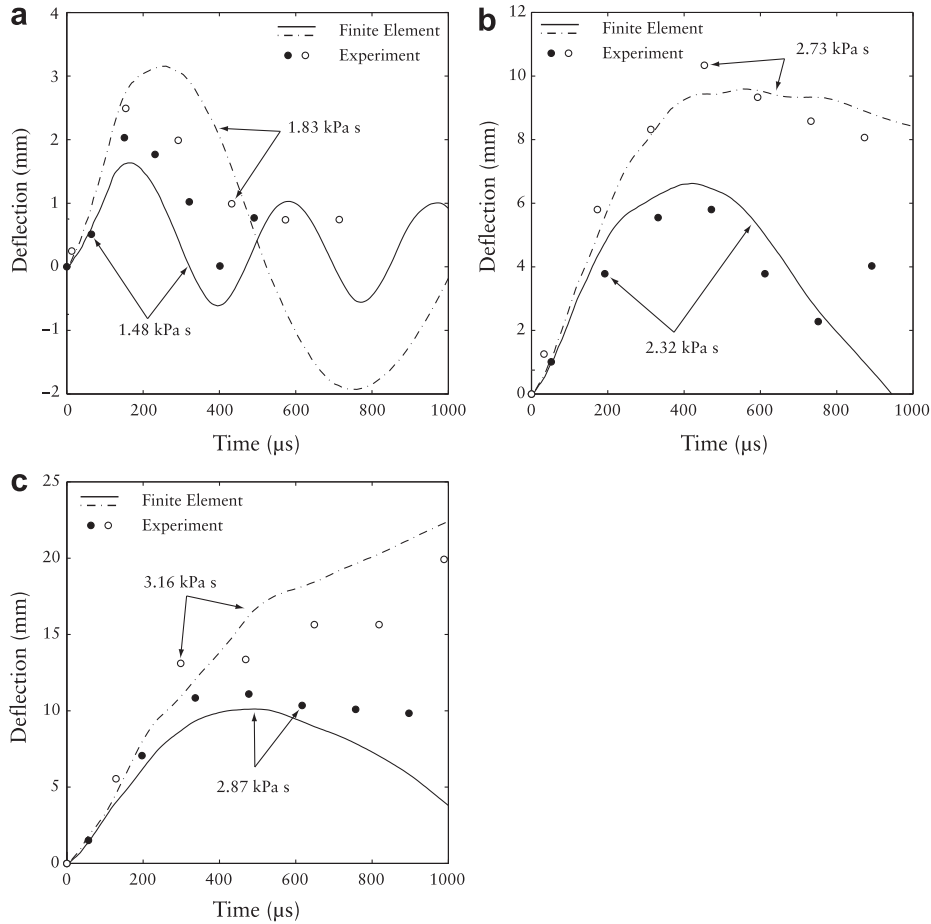


Fig. 5. The measured deflections (from the high speed images) of the back face of the sandwich beams at mid-span as a function of time t for the six levels of impulse I_0 investigated here. (a) $I_0 = 1.48$ kPa s and 1.83 kPa s, (b) 2.32 kPa s and 2.73 kPa s and (c) 2.87 kPa s and 3.16 kPa s. Time $t = 0$ corresponds to the instant that the metal foam projectile impacts the beam. Predictions from the FE analysis are included for each case.

contact between the projectile and front face sheet. The general contact algorithm in ABAQUS enforced hard, no-friction contact interaction using a penalty algorithm. Clamped boundary conditions were imposed on the ends of the beams by constraining all degrees of freedom, such that the free span was $l = 200$ mm.

In the FE model, the monolithic and sandwich beams were constructed from an assembly of unidirectional laminates as follows. First consider the sandwich beams. The composite sandwich beams were modelled using 4-noded shell elements with reduced integration (S4R in the ABAQUS notation). Each ply of the face sheets was attached to its neighbour via a cohesive surface in order to allow for the possibility of delamination within the face sheets. Recall that the webs of the square-honeycomb core comprised a single layer of the woven composite material of thickness $t_c = 0.35$ mm with fibres at $\pm 45^\circ$ with respect to the x_3 axis of the beam (Fig. 1). These were modelled as a pair of orthogonal plies of thickness $t_c/2$ tied together; the woven construction of the core webs prevented them from delaminating. The cell size L , core height H and number of webs of the square-honeycomb core matched the test configuration; the webs of the core were bonded to the face sheets via an adhesive layer modelled as an isotropic J2 elastic-plastic solid.

Second, consider the monolithic beams. They were modelled as 15 unidirectional plies with alternating 0° and 90° fibre orientations. Again, the plies were attached to each other via a cohesive surface in order to account for delamination.

4.2. Brief description of the constitutive model for each composite ply

Consider a single ply of a fibre reinforced unidirectional laminate with the x_1 axis in the fibre direction, x_2 in the transverse direction and x_3 perpendicular to the plane of the ply, as sketched in Fig. 10. The unidirectional ply is transversely isotropic with respect to the fibre direction (the x_1 axis). For a state of plane stress ($\sigma_{33} = \sigma_{32} = \sigma_{13} = 0$), the elastic response of the *undamaged* material is given by

$$\begin{pmatrix} \varepsilon_{11} \\ \varepsilon_{22} \\ \gamma_{12} \end{pmatrix} = \begin{pmatrix} 1/E_1 & -\nu_{21}/E_1 & 0 \\ -\nu_{12}/E_2 & 1/E_2 & 0 \\ 0 & 0 & 1/G \end{pmatrix} \begin{pmatrix} \sigma_{11} \\ \sigma_{22} \\ \sigma_{12} \end{pmatrix} \quad (4.1)$$

where ε_{11} and ε_{22} are the direct strains in the x_1 and x_2 directions, respectively, and γ_{12} is the engineering shear strain. The Young's moduli E_1 and E_2 in the x_1 and x_2 directions, along with the shear modulus G and Poisson's ratio ν_{21} are the four relevant elastic constants of the unidirectional laminate while the Poisson's ratio ν_{12} is not an independent elastic constant and related to the other elastic constants via the relation $\nu_{21} = (E_2/E_1)\nu_{12}$.

4.2.1. The damage law

The laminate is taken to be linear elastic as specified by Eq. (4.1) up to the initiation of damage. As damage progresses there is a drop in the three moduli (E_1 , E_2 , G) with increasing strain, and stress versus strain response becomes non-linear. Four scalar damage

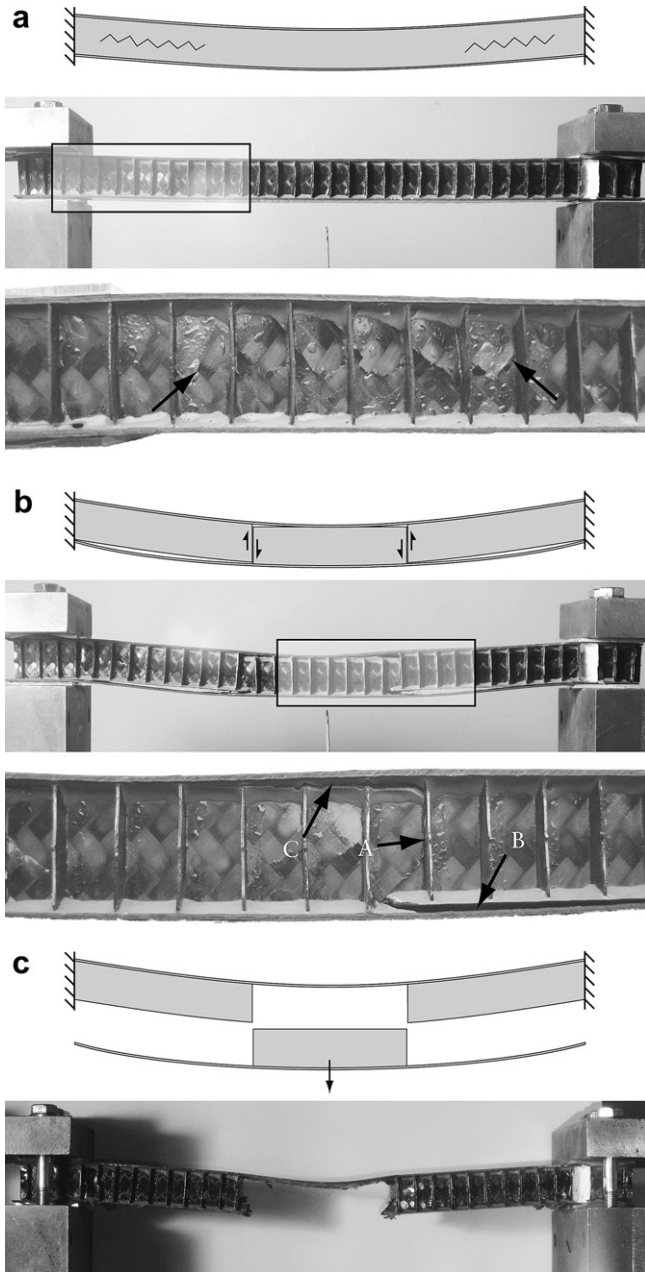


Fig. 6. Images of the as-tested sandwich beams for three levels of the applied impulse that show 3 of the observed failure modes. (a) Fracture of the core along the neutral axis of the beam for $I_0 = 2.66$ kPa s. (b) Plug-type shear failure of the core at the edges of the impact site for $I_0 = 2.82$ kPa s and (c) complete debonding of the back face leading to complete failure of the beams for $I_0 = 3.18$ kPa s.

variables d_i are introduced, corresponding to four damage modes (tensile and compressive failure in each of the fibre and transverse directions). In the undamaged state each damage variable is set to zero. Rate-controlled-damage accumulates with strain and the moduli drop with increasing value of the damage variables, such that one or more moduli equal zero when one of the damage variables attains unity.

The damage model has two elements, as follows.

- Damage can only accumulate when a critical stress state is attained or exceeded, as proposed by Hashin [22]; the damage locus is a function of the current value of scalar damage variables d_i . For a stress state within the damage locus, no additional damage occurs and the stress versus strain response is linear and reversible, with current elastic moduli that depend only upon d_i . As the d_i increase with time, the elastic moduli and the magnitude of the damage locus diminish.
- The damage variables d_i evolve with time according to a set of first order differential equations, with the driving term in these equations given by an additional set of rate-independent damage variables D_i . The variables D_i depend upon the strain state following the prescription of Matzenmiller et al. [21].

The motivation for introducing the time-dependent damage parameters d_i in addition to the more standard variables D_i is to account for the rate-dependent strength of the laminate. We shall demonstrate below that this is needed in order to capture the observed response.

4.2.2. The damage locus

We denote the tensile and compressive strengths for damage initiation in the undamaged laminate and in the fibre direction (x_1 -direction) by X^T and X^C , respectively. The corresponding tensile and compressive strengths in the transverse direction are denoted by Y . After damage has developed these strengths drop as follows. Write the damage variable for tensile failure in the fibre direction as d_f^t . Then, the current tensile strength in the fibre direction is $(1 - d_f^t)X^T$. Likewise, the damage variables for compressive loading in the fibre direction is d_m^c , while that for transverse tension and compression is d_m^t and d_m^c , respectively. No additional damage develops when the stress state lies within the following critical surfaces:

$$\frac{\langle \sigma_{11} \rangle}{(1 - d_f^t)X^T} < 1 \quad (4.2)$$

$$\frac{\langle -\sigma_{11} \rangle}{(1 - d_m^c)X^C} < 1 \quad (4.3)$$

$$\left(\frac{\langle \sigma_{22} \rangle}{(1 - d_m^t)Y} \right)^2 + \left(\frac{2\sigma_{12}}{(1 - d_s)Y} \right)^2 < 1 \quad (4.4)$$

and

$$\left(\frac{\langle -\sigma_{22} \rangle}{(1 - d_m^c)Y} \right)^2 + \left(\frac{2\sigma_{12}}{(1 - d_s)Y} \right)^2 < 1 \quad (4.5)$$

where $\langle \rangle$ represents the Macaulay bracket of value zero when its argument is negative. The shear damage d_s is defined as

$$d_s \equiv 1 - (1 - d_f^t)(1 - d_f^c)(1 - d_m^t)(1 - d_m^c) \quad (4.6)$$

In any given state of damage, the secant relationship between stress and strain reads

$$\begin{pmatrix} \varepsilon_{11} \\ \varepsilon_{22} \\ \gamma_{12} \end{pmatrix} = \begin{pmatrix} 1/[E_1(1 - d_f)] & -\nu_{21}/[E_1(1 - d_f)(1 - d_m)] & 0 \\ -\nu_{12}/[E_2(1 - d_m)(1 - d_f)] & 1/[E_2(1 - d_m)] & 0 \\ 0 & 0 & 1/[G(1 - d_s)] \end{pmatrix} \begin{pmatrix} \sigma_{11} \\ \sigma_{22} \\ \sigma_{12} \end{pmatrix} \quad (4.7)$$

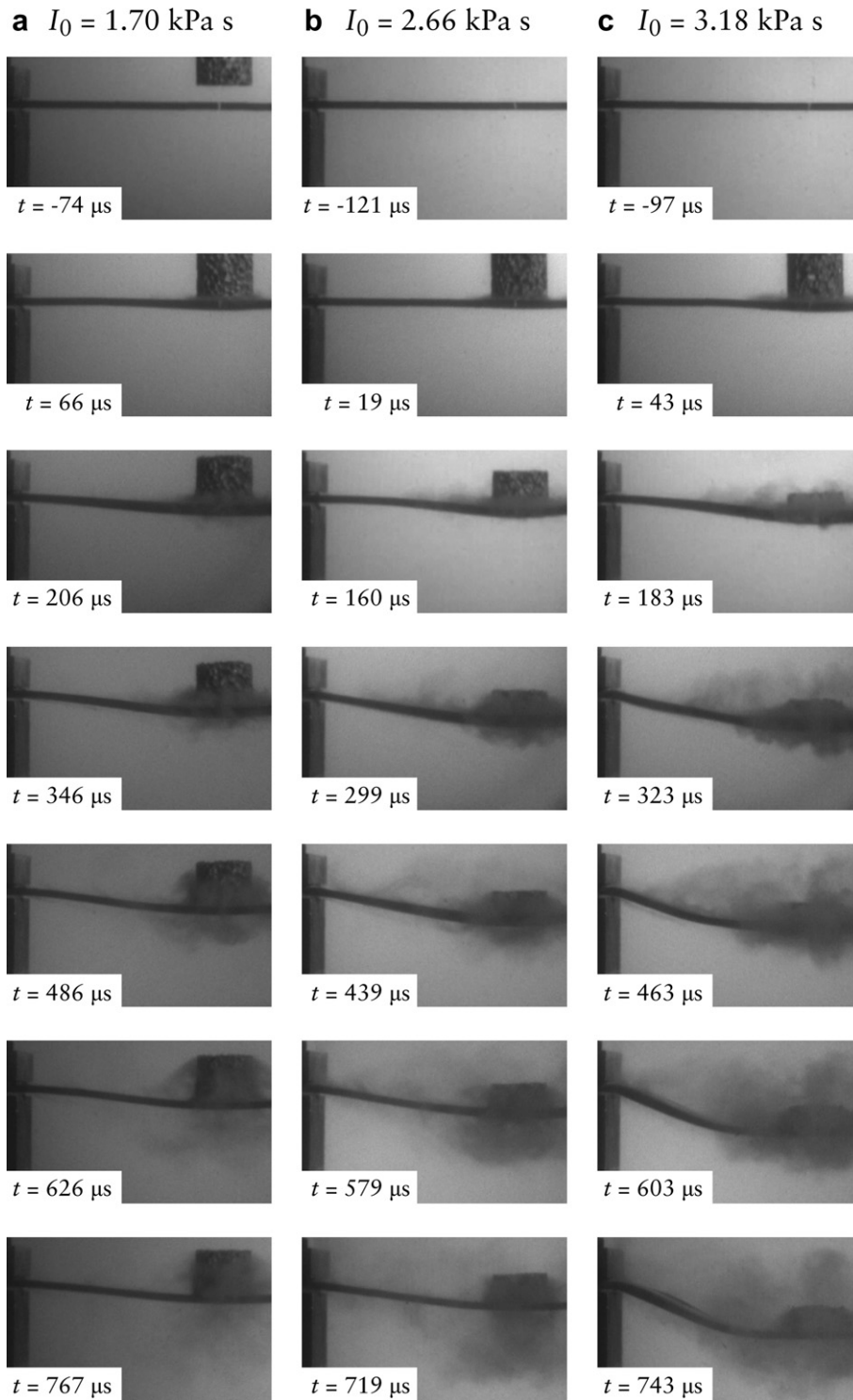


Fig. 7. Montage of high speed images showing the observed sequence of deformation of the monolithic beams subjected to three levels of impulse I_0 (a) 1.70 kPa s, (b) 2.66 kPa s and (c) 3.18 kPa s via the metal foam impact. Time $t = 0$ corresponds to the instant that the metal foam projectile impacts the beam.

where

$$d_f = \begin{cases} d_f^t & \text{if } \sigma_{11} \geq 0 \\ d_f^c & \text{otherwise} \end{cases}$$

and

$$d_m = \begin{cases} d_m^t & \text{if } \sigma_{22} \geq 0 \\ d_m^c & \text{otherwise} \end{cases}$$

(4.8)

We note from Eqs. (4.7) and (4.8) that if the composite is fully damaged in say the compressive fibre damage mode, it can still sustain tensile fibre stresses. The validity of this assumption remains to be verified experimentally but is not expected to affect the results here significantly as most material elements undergo proportional loading.

The evolution law for the steady-state values of the damage variables is now summarised for each of the four independent

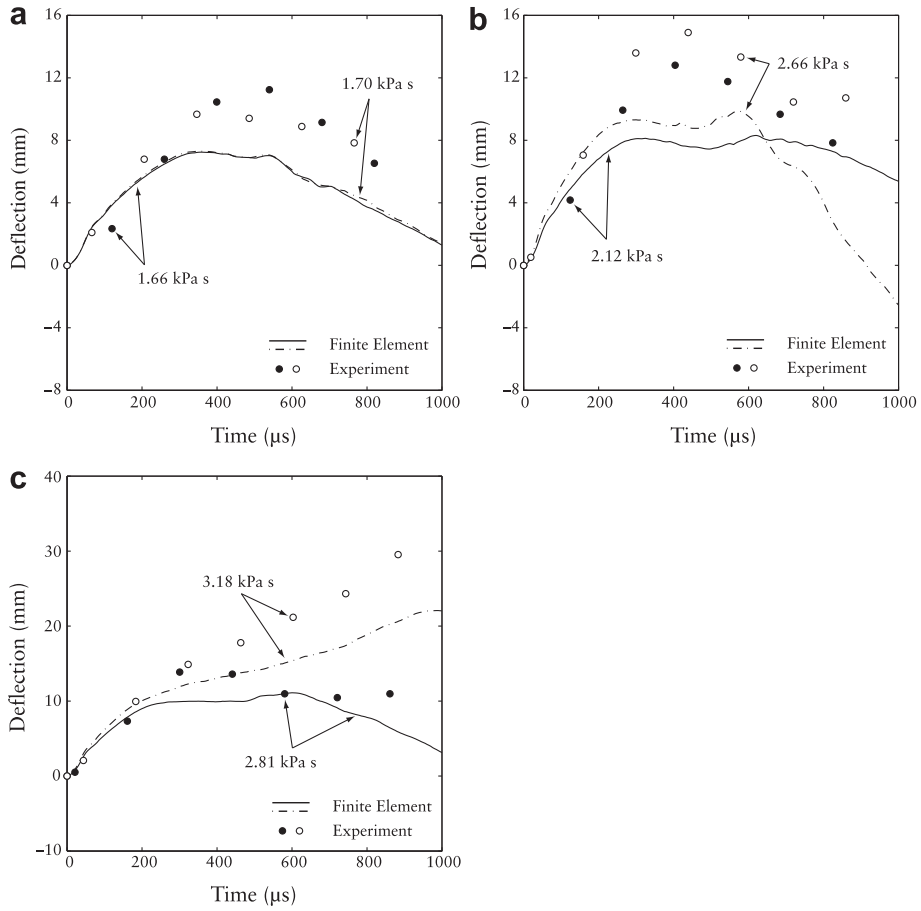


Fig. 8. The measured deflections (from the high speed images) of the monolithic beams at mid-span as a function of time t for the six levels of impulse I_0 investigated here. (a) $I_0 = 1.66$ kPa s and 1.70 kPa s, (b) 2.12 kPa s and 2.66 kPa s and (c) 2.81 kPa s and 3.18 kPa s. Time $t = 0$ corresponds to the instant that the metal foam projectile impacts the beam. Predictions from the FE analysis are included for each case.

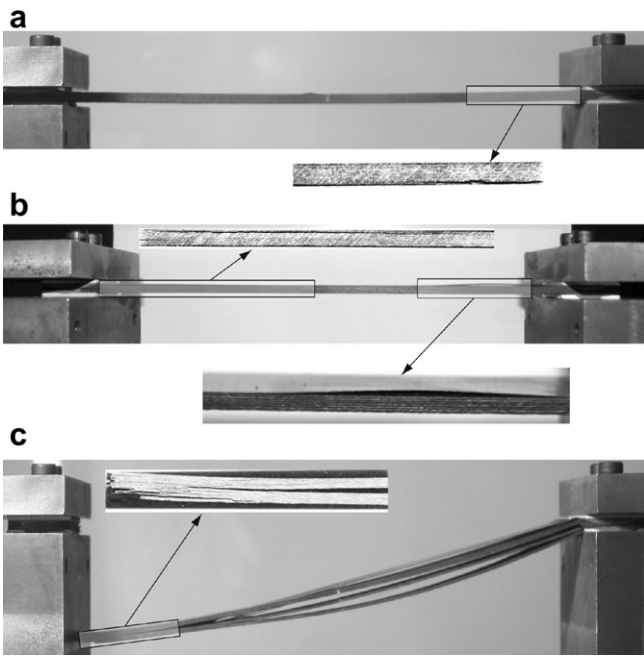


Fig. 9. Selected images of the as-tested monolithic beams to illustrate the observed failure mechanisms. (a) Delamination near the supports $I_0 = 2.66$ kPa s. (b) Delamination over the entire beam span at $I_0 = 2.81$ kPa s and (c) fibre fracture at the supports at impulses $I_0 = 3.18$ kPa s. Delamination is seen as dark patches in the photographs.

damage variables d_f^t , d_f^c , d_m^t and d_m^c , with the corresponding rate-independent reference values denoted by D_f^t , D_f^c , D_m^t and D_m^c , respectively. The damage growth law adopted here is based upon the assumption that the stress decreases linearly with increasing strain once damage initiates. First, consider the tensile fibre damage mode. An effective strain ϵ_f^t is defined as $\epsilon_f^t \equiv \langle \epsilon_{11} \rangle$ and is used to update the damage state variable via the relation

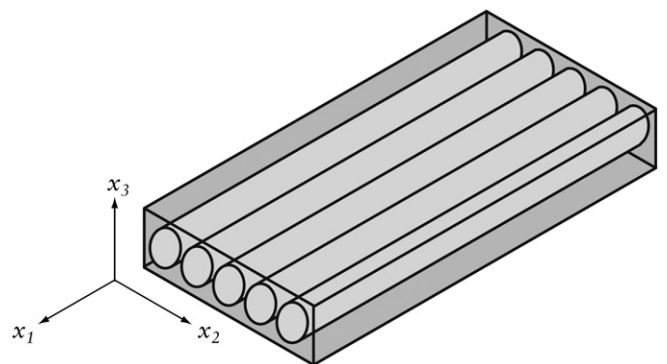


Fig. 10. Sketch illustrating the co-ordinate system for a single ply of a unidirectional laminate.

$$D_f^t = \frac{2J_f^t (\hat{\varepsilon}_f^t - X^T/E_1)}{\hat{\varepsilon}_f^t \left(\frac{2J_f^t}{L_e X^T} - X^T/E_1 \right)} \leq 1 \quad (4.9)$$

where X^T/E_1 is the value of $\hat{\varepsilon}_f^t$ when tensile fibre first initiates and $2J_f^t/L_e X^T$ is the strain for complete tensile fibre damage. Here, J_f^t is the tensile fibre fracture energy and L_e is a representative length scale. We note in passing that an additional constraint must be imposed upon Eq. (4.9) for it to be meaningful: $\dot{D}_f^t \geq 0$, reflecting that fact that damage is irreversible. When the axial strain is decreased we hold D_f^t fixed.

Similarly, the compressive fibre damage variable is specified as

$$D_f^c = \frac{2J_f^c (\hat{\varepsilon}_f^c - X^c/E_1)}{\hat{\varepsilon}_f^c \left(\frac{2J_f^c}{L_e X^c} - X^c/E_1 \right)} \leq 1 \quad (4.10)$$

where J_f^c is the compressive fibre fracture energy and the effective strain is $\hat{\varepsilon}_f^c \equiv \langle -\varepsilon_{11} \rangle$. The matrix damage variables are given by

$$D_m^t = \frac{2J_m (\hat{\varepsilon}_m^t - Y/E_2)}{\hat{\varepsilon}_m^t \left(\frac{2J_m}{L_e Y} - Y/E_2 \right)} \leq 1 \quad (4.11)$$

and

$$D_m^c = \frac{2J_m (\hat{\varepsilon}_m^c - Y/E_2)}{\hat{\varepsilon}_m^c \left(\frac{2J_m}{L_e Y} - Y/E_2 \right)} \leq 1 \quad (4.12)$$

where J_m is the matrix fracture energy and the effective strains are defined as $\hat{\varepsilon}_m^t \equiv \sqrt{\langle \varepsilon_{22} \rangle^2 + \varepsilon_{12}^2}$ and $\hat{\varepsilon}_m^c \equiv \sqrt{\langle -\varepsilon_{22} \rangle^2 + \varepsilon_{12}^2}$. In this study, we choose L_e to be the mesh size of a finite element; numerical experimentation confirmed that this choice gives a response which is almost independent of mesh size.

Finally, the current value of the each of the damage variables is specified via a rate law. For example, the tensile fibre damage variable is specified as the solution to the first order differential equation

$$\dot{d}_f^t = \frac{1}{\tau} (D_f^t - d_f^t) \quad (4.13)$$

where τ is a time-constant that governs the rate at which d_f^t attains its steady-state value D_f^t . Analogous relations are defined for the other three damage variables with the value of the time-constant equal for all the damage modes.

Based on the measured quasi-static properties of the laminated composites, the material parameters for the plies comprising the sandwich beam face sheets and the monolithic beams are listed in Table 1. Except for τ all parameters are directly measured by quasi-static measurements. The rate sensitivity of the composite response is included via the time-constant τ : while this rate sensitive response was not directly measured, the value of τ listed in Table 1 has been chosen so as to give accurate predictions of the sandwich and monolithic measurements over the whole range of impact velocities investigated here. We shall subsequently show that, absent rate sensitivity, the FE simulations grossly over-predict the observed deflections. It is also necessary to specify the densities of

Table 1

The material properties of each unidirectional ply of the woven and laminate composite materials employed in the constitutive model in the FE calculations.

Material	Property	Value	
Woven	E_1 (GPa)	126	
	E_2 (GPa)	5.1	
	G (GPa)	4.7	
	ν_{12}	0.2	
	X^T (MPa)	1080	
	X^c (MPa)	660	
	Y (MPa)	160	
	J_f^t/L_e (MPa)	5.6	
	J_f^c/L_e (MPa)	2.1	
	J_m/L_e (MPa)	9.6	
	ply thickness (mm)	0.175	
	Density (kg m^{-3})	1370	
	τ (μs)	8	
	Laminate	E_1 (GPa)	170
		E_2 (GPa)	5.1
G (GPa)		4.7	
$\nu_{12} = \nu_{21}$		0.15	
X^T (MPa)		1960	
X^c (MPa)		1260	
Y (MPa)		160	
J_f^t/L_e (MPa)		13.6	
J_f^c/L_e (MPa)		5.6	
J_m/L_e (MPa)		9.6	
ply thickness (mm)		0.25	
Density (kg m^{-3})		1570	
τ (μs)		6	

the composite sheets due to the dynamic nature of the simulations and experiments. Consistent with the measurements, the densities of the woven core and laminate face sheet materials were taken as 1370 kg m^{-3} and 1570 kg m^{-3} , respectively. Readers are referred to Russell et al. [20] for further details regarding the calibration of the material model. It is worth emphasizing here that Russell et al. [20] have demonstrated that this composite material model, using the material parameters as listed in Table 1 but with $\tau = 0$, predicted the deformation and failure of a range of sandwich beams geometries under quasi-static loading to a high level of accuracy, thus confirming the fidelity of the model under static conditions.

The predictions of the tensile/compressive responses for the laminate and woven materials are included in Fig. 3a and b, respectively, for both the 0° – 90° and $\pm 45^\circ$ orientations. The agreement with measurements for the 0° – 90° orientation is excellent in terms of the modulus, peak strength and post peak responses. However, in the $\pm 45^\circ$ orientation the measured response does not display a linear softening behaviour as assumed in the damage evolution laws detailed here. Thus, while the model accurately captures the initial elastic response and peak strength it does not model the entire stress versus strain curve to high fidelity.

4.3. Cohesive law for the interface between plies

The unidirectional plies in the face sheets of the sandwich beams and in the monolithic beams were attached to each other via a cohesive surface. This cohesive surface simulates the traction versus separation behaviour of the plies and permits the FE model to include possible delamination of the plies.

Define the normal traction between the plies as t_n and the two shear tractions as t_t and t_s . The corresponding normal and shear separations are denoted by δ_n , δ_t and δ_s . The cohesive relationship is defined in two steps: (i) the undamaged traction–separation relation and (ii) a softening relation after the onset of damage.

At any given instant, the traction versus separation relation is of the form

$$\begin{aligned}
 t_n &= \begin{cases} (1-D)k_n\delta_n & \delta_n > 0 \\ k_n\delta_n & \text{otherwise} \end{cases} \\
 t_s &= (1-D)k_s\delta_s \\
 t_t &= (1-D)k_t\delta_t
 \end{aligned} \tag{4.14}$$

where k_n and k_s are the normal and shear stiffnesses, respectively and the damage variable $0 \leq D \leq 1$. Note that damage does not affect the cohesive relation when $\delta_n \leq 0$, i.e. in compression the interaction between two plies reduces to a penalty contact algorithm. In the undamaged state (at the beginning of the calculation) the damage variable $D = 0$ and no additional damage develops when the traction state lies within the following surface

$$\left[\frac{\langle t_n \rangle}{(1-D)T_n} \right]^2 + \left[\frac{t_s}{(1-D)T_s} \right]^2 + \left[\frac{t_t}{(1-D)T_t} \right]^2 < 1 \tag{4.15}$$

where T_n and T_s represent the peak values of the traction when the separation is either purely normal or pure shear, respectively. The evolution law for D is based upon the assumption that the tractions decrease linearly with increasing separation once damage has initiated. Define an effective separation by

$$\delta_e \equiv \sqrt{\langle \delta_n \rangle^2 + \delta_s^2 + \delta_t^2} \tag{4.16}$$

The work-conjugate traction to this effective separation is

$$t_e \equiv \sqrt{\langle t_n \rangle^2 + t_s^2 + t_t^2} \tag{4.17}$$

The damage variable D is then defined in terms of the fracture energy G_c as

$$D = \frac{\frac{2G_c}{t_e^0} (\delta_e^{\max} - \delta_e^0)}{\delta_e^{\max} \left(\frac{2G_c}{t_e^0} - \delta_e^0 \right)} \leq 1, \tag{4.18}$$

where δ_e^{\max} is the maximum value of δ_e attained during the loading history while t_e^0 and δ_e^0 are the values of the effective traction and

Table 2

Material parameters for the cohesive surface between the plies of the laminate material used to model delamination in the FE calculations.

Property	Value
k_n	5.12 GPa mm ⁻¹
k_s	4.72 GPa mm ⁻¹
T_n	320 MPa
T_s	160 MPa
G_c	5150 J m ⁻²

separation at the initiation of damage. This interface relationship was assumed to be rate insensitive.

The material parameters that define the interface model are the stiffnesses k_n and k_t , maximum tractions T_n and T_s as well as the fracture energy G_c . The values of these five parameters are listed in Table 2. They have been estimated as follows:

- We assume that the interface between the plies is a 0.1 mm thick layer of the HexPly® 8552 resin. The parameters k_n , k_s , T_n and T_s are then estimated from the manufacturers data on the tensile and shear properties of the resin.
- The fracture energy G_c was not directly measured but taken to be similar to that of epoxy resins; see for example data for the redux 319 material [26].

We emphasize here that this cohesive law is a mixed mode law that is characterised by a single fracture energy G_c .

4.4. Model of the adhesive layer between core and face sheets

The adhesive layer bonding the webs of the core to the face sheets was included in the FE model as an additional layer of thickness $\Delta t = 0.4$ mm and width $\Delta w = 1.1$ mm connecting the composite webs of the core to the face sheets, as shown in Fig. 11. This adhesive layer was modelled as a J2-flow theory elastic-plastic material with Young’s modulus E , Poisson’s ratio ν and uniaxial tensile yield strength σ_Y^0 . In order to model possible debonding of the core from the face sheets, damage initiation and evolution of

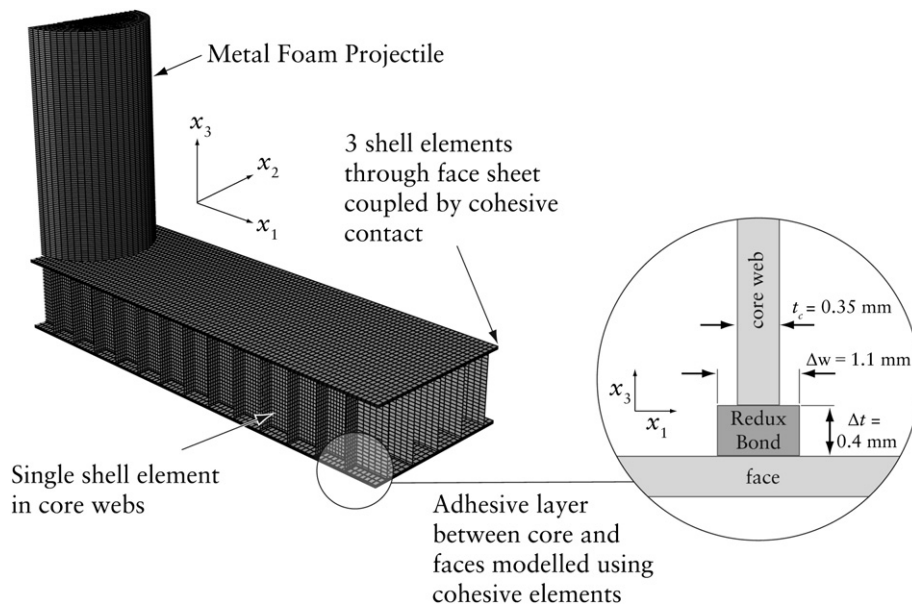


Fig. 11. Sketch illustrating the adhesive joint between the sandwich core and the face sheets as modelled in the FE analysis.

the adhesive was included into the material definition as follows. Damage was assumed to initiate when the von Mises effective plastic strain reached a critical value ε_c . Subsequently, the damage variable $0 \leq d \leq 1$ was assumed to evolve according to the relation

$$\dot{d} = \frac{L_e \sigma_Y^0}{2G_f} \dot{\varepsilon}^{pl} \quad (4.19)$$

where L_e is a characteristic element size, G_f the fracture energy and $\dot{\varepsilon}^{pl}$ the von-Mises effective plastic strain rate. The damage variable was set to $d = 0$ before the initiation of damage and it reduces the yield strength of the adhesive according to the relation $(1 - d) \sigma_Y^0$.

The manufacturers data sheet for the Redux 319 gave the density of the adhesive as 1100 kg m^{-3} along with $E = 4.35 \text{ GPa}$, $\nu = 0.36$, $\sigma_Y^0 = 75 \text{ MPa}$, $\varepsilon_c = 0.048$ and $G_f = 1460 \text{ J m}^{-2}$. The characteristic element size L_e was taken to be the adhesive width Δw .

4.5. Material model for the metal foam projectile

The Alporas aluminium foam projectiles were modelled as a compressible continuum using the metal foam constitutive model of Deshpande and Fleck [27]. Write s_{ij} as the usual deviatoric stress and the von Mises effective stress as $\sigma_e \equiv \sqrt{3s_{ij}s_{ij}/2}$. Then, the isotropic yield surface for the metal foam is specified by

$$\hat{\sigma} - Y = 0. \quad (4.20)$$

where the equivalent stress $\hat{\sigma}$ is a homogeneous function of σ_e and mean stress $\sigma_m \equiv \sigma_{kk}/3$ according to

$$\hat{\sigma}^2 \equiv \frac{1}{1 + (\alpha/3)^2} [\sigma_e^2 + \alpha^2 \sigma_m^2]. \quad (4.21)$$

The material parameter α denotes the ratio of deviatoric strength to hydrostatic strength, and the normalisation factor on the right hand side of relation Eq. (4.21) is chosen such that $\hat{\sigma}$ denotes the stress in a uniaxial tension or compression test. An over-stress model is employed with the yield stress Y specified by

$$Y = \mu \dot{\varepsilon}^p + \sigma_c, \quad (4.22)$$

in terms of the viscosity μ , and the plastic strain-rate $\dot{\varepsilon}^p$ (work conjugate to $\hat{\sigma}$). $\sigma_c(\dot{\varepsilon}^p)$ is the static uniaxial stress versus plastic strain relation. Normality of plastic flow is assumed, and this implies that the ‘‘plastic Poisson’s ratio’’ $\nu_p = -\dot{\varepsilon}_{22}^p/\dot{\varepsilon}_{11}^p$ for uniaxial compression in the 1-direction is given by

$$\nu_p = \frac{1/2 - (\alpha/3)^2}{1 + (\alpha/3)^2} \quad (4.23)$$

In the simulations, the Alporas foam is assumed to have a Young’s modulus $E_c = 1.0 \text{ GPa}$, an elastic Poisson’s ratio $\nu = 0.3$ and a plastic Poisson’s ratio $\nu_p = 0$ (i.e. $\alpha = 3/\sqrt{2}$) [28]. Consistent with quasi-static measurements of the Alporas foam response, the static uniaxial yield strength σ_c versus equivalent plastic strain $\dot{\varepsilon}^p$ history is approximated to be bi-linear and of the form

$$\sigma_c = \begin{cases} \sigma_{pl} & \dot{\varepsilon}^p \leq -\ln(1 - \varepsilon_D) \\ \text{otherwise} & \end{cases} \quad (4.24)$$

where the plateau strength of the foam is $\sigma_{pl} = 2.5 \text{ MPa}$ and the nominal densification strain $\varepsilon_D = 0.75$. This isotropic hardening model assumes that hardening under all strain paths is characterised by Eq. (4.24). Recall that the length of the foam projectile is $l_0 = 50 \text{ mm}$. The viscosity μ was set so that the shock width w has the value of $l_0/10$, where [17]

$$w = \frac{\mu \varepsilon_D}{\rho_p \Delta v}, \quad (4.25)$$

in terms of the initial foam density $\rho_p = 200 \text{ kg m}^{-3}$ and the velocity jump Δv across the shock. Now Δv is on the order of the projectile velocity v_0 , and so the predicted shock width $w = 5 \text{ mm}$, which is of similar magnitude to that observed in shock experiments [17]. Large gradients in stress and strain occur over the shock width and thus a mesh size of 1 mm was used for discretisation of the foam projectile, in order to resolve these gradients accurately.

5. Comparison of the measurements and FE simulations

The FE mesh of the sandwich beams comprised approximately square elements of size 1.2 mm in each ply of the face sheets and 0.7 mm in the webs of the core. This element size is used as L_e in the damage variables specified in Section 4 in order to ensure an approximately mesh size independent response: choosing L_e to be larger or smaller than the actual mesh size gives results that are mesh size dependent. The Matzenmiller et al. [21] and Hashin [22] model for the initiation and development of damage in unidirectional fibre composites is one of the standard models in the commercial ABAQUS FE code and we employ this implementation in the simulations along with the element removal option in ABAQUS: an element representing the composite sheets was removed from the calculation when all four independent damage variables within that element attain their maximum value of unity and the element was no longer able to sustain any stress. Similarly, the elements representing the Redux adhesive were also removed when the damage variable of the adhesive attained a value of unity. A mesh sensitivity study was performed to ensure that the finite element meshes were fine enough to give converged results. Note that the calculations display some mesh size sensitivity once damage occurs due to the softening nature of the response. However, this mesh size sensitivity is greatly alleviated by choosing the representative length scale L_e to equal the characteristic mesh size. Similarly, each ply of the monolithic beams was discretised by square elements of size 1.2 mm . The foam projectiles had approximately 50 elements in the axial direction and 14 elements along the radius.

Unless otherwise specified, all FE results are presented using the reference material properties as specified in Section 4. Comparisons are presented first for the sandwich beams and then for the monolithic composite beams.

5.1. Sandwich beams

A comparison between the measurements and FE predictions of the deflections of the mid-span of the back face of the sandwich beams as a function of time t after the impact is included in Fig. 5 for the six impulse levels investigated here. The predictions are reasonably accurate over the entire range of impulses. The largest discrepancies are at the lower impulses $I_0 \leq 1.83 \text{ kPa s}$ when the deflections are typically on the order of 2 mm . Deflections of less than about 1 mm cannot be resolved from the high speed images and thus there is some uncertainty in the measurements of the deflections at these low impulse levels. This is the primary reason for the discrepancy. However, the FE calculations accurately predict: (i) the beams remain essentially elastic for $I_0 \leq 1.83 \text{ kPa s}$ with no residual permanent deflection and (ii) the beams undergo complete separation from the supports and deflections become unbounded at $I_0 \leq 3.16 \text{ kPa s}$.

Predictions of the transient deformation response for $I_0 \leq 2.73 \text{ kPa s}$ and 3.16 kPa s are included in Fig. 12. The deformed

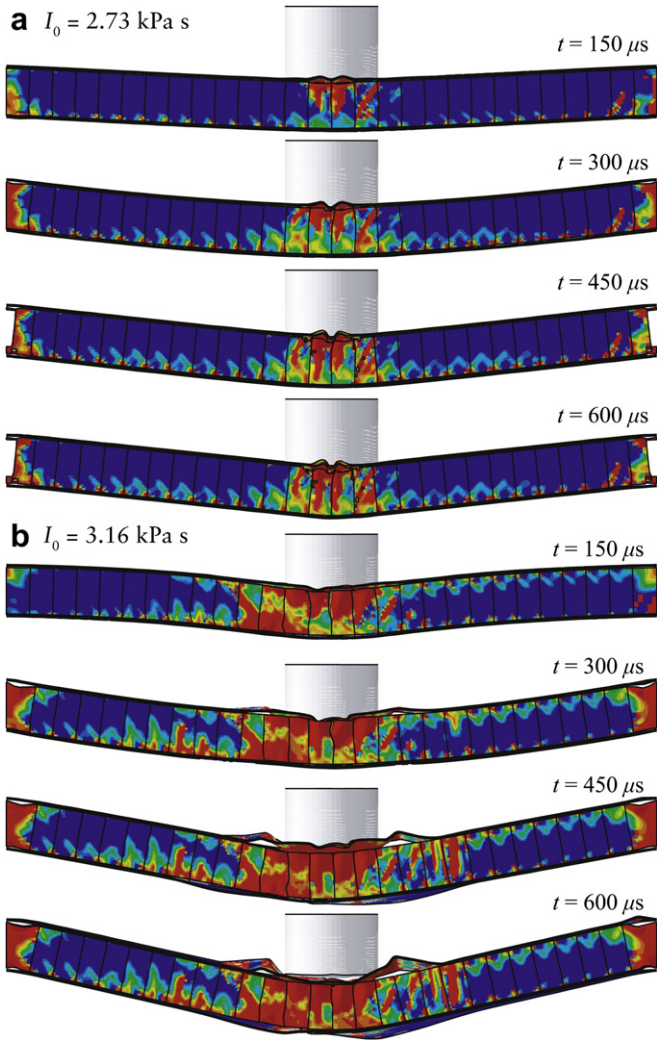


Fig. 12. FE predictions of the temporal variation of the deformation of the sandwich beams subjected to the metal foam impact for (a) $I_0 = 2.73$ kPa s and (b) 3.16 kPa s. The plots are shaded with predictions of the damage variable d_s with time $t = 0$ corresponding to the instant that the metal foam projectile impacts the beam.

FE meshes contain contours of the damage variable d_s as defined in Eq. (4.6); this damage variable indicates damage by any of the four composite damage modes. The predicted modes are in good

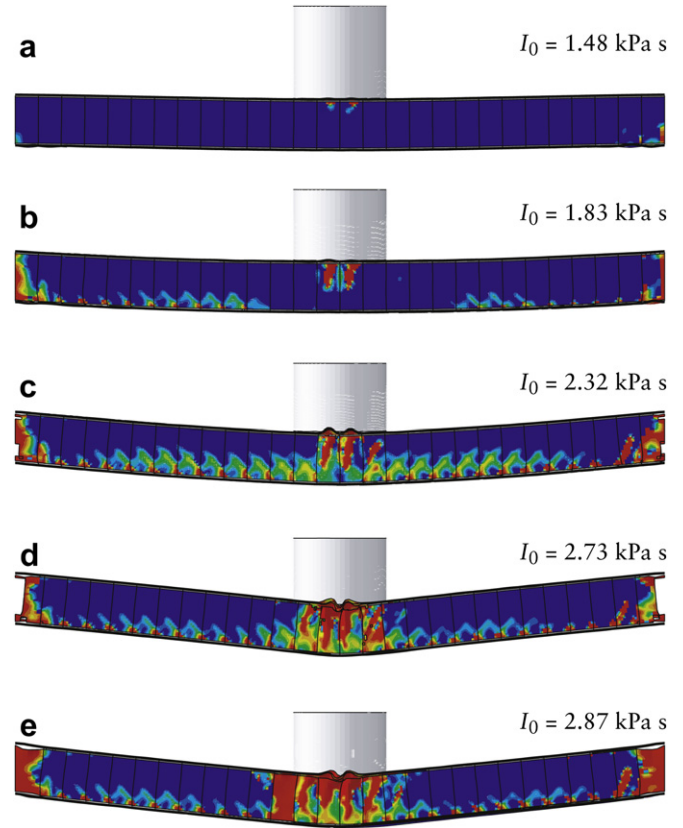


Fig. 13. FE predictions of the deformed shapes at peak deflections for five impulses (a) $I_0 = 1.48$ kPa s, (b) $I_0 = 1.83$ kPa s, (c) 2.32 kPa s, (d) 2.73 kPa s and (e) 2.87 kPa s. The plots are shaded with predictions of the damage variable d_s .

agreement with the observations in Fig. 4 including the following features: (i) deformation has spread over the entire beam span by 50 μ s, (ii) extensive core damage occurs immediately beneath the impact site for $I_0 \leq 3.16$ kPa s and (iii) face-sheet delamination occurs at $I_0 \leq 3.16$ kPa s but not at the lower impulse of 2.73 kPa s.

The predicted damage state d_s at peak deflection of the sandwich beams are given in Fig. 13 for the five impulses $I_0 \leq 2.87$ kPa s. The images clearly show that negligible damage occurs for $I_0 \leq 1.83$ kPa s, and this is consistent with the fact that the beams remain essentially elastic at $I_0 \leq 1.83$ kPa s. With increasing I_0 ,

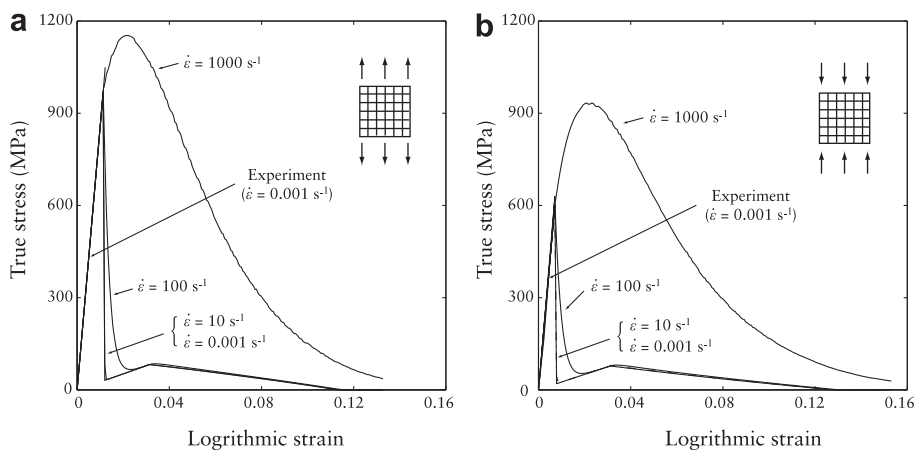


Fig. 14. FE predictions of the uniaxial (a) tensile and (b) compressive responses of the laminate material in the 0° – 90° orientation for selected applied strain rates ranging from quasi-static to 1000 s^{-1} . The material time constant is chosen to be $\tau = 8$ s.

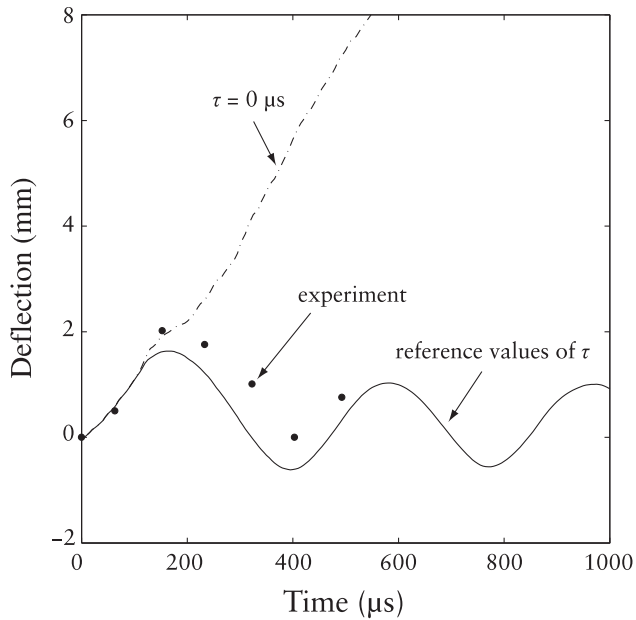


Fig. 15. FE predictions of the temporal variation of the back face deflection (at mid-span) of the sandwich beam subjected to an impulse $I_0 = 1.48$ kPa s. The predictions are included with material rate sensitivity switched-off (i.e. $\tau = 0$) and the reference values of τ for the face sheet and core materials. The corresponding measurements are included in the figure.

damage increases beneath the impact site and builds up near the supports. Further, face-sheet delamination occurs over the central section of the beam. These predictions are consistent with the observations in Fig. 6.

5.1.1. Effect of material rate sensitivity

The above predictions assume a rate sensitive composite response as characterised by the time-constant τ in Eq. (4.13). In order to assess the significance of rate sensitivity, predictions of the uniaxial tensile and compressive responses of the [0/90] laminate are given in Fig. 14 for strain rates ranging from quasi-static to 1000 s^{-1} , and τ set to the reference value of 8 μs . The predicted response is relatively rate insensitive over the strain rate range 10^{-3} s^{-1} to 100 s^{-1} and agrees well with the measured quasi-static response. However, there is a significant enhancement in the tensile and compressive strengths as well as ductility for an applied strain rate of 1000 s^{-1} . These enhanced high strain rate properties

have a significant influence on the FE predictions of the dynamic responses of the beams.

The FE prediction of the dynamic response (mid-span deflection versus time) of the sandwich beam subjected to an impulse $I_0 = 1.48$ kPa s via the metal foam impact is plotted in Fig. 15 with material rate sensitivity of both the laminate face sheet material and the woven core material switched-off (i.e. $\tau = 0$). The corresponding measured response and FE predictions with the reference values of τ are included in Fig. 15. Recall that $I_0 = 1.48$ kPa s is the lowest impulse tested in this study and the observed beam response was essentially elastic with no residual deflection or observable damage. However, while the FE calculations with the reference values of τ are in good agreement with the measurements, the predictions with $\tau = 0$ predict failure of the beam with unbounded deflections. This clearly illustrates the significance of material rate sensitivity in enhancing the dynamic performance of the composite material.

5.2. Monolithic beams

Predictions of the mid-span deflections versus time histories of the monolithic beams are included in Fig. 8 for the six levels of impulse investigated here. While the FE predictions predict the general trends with reasonable accuracy, including the failure of the beams at the supports for an impulse $I_0 = 3.18$ kPa s, they under-predict the peak deflections by about 20% especially at the lower impulses. Further, the FE calculations predict partial delamination over the entire impulse range while in the experiments delamination was only observed for impulses $I_0 \geq 2.7$ kPa s. However, we shall show subsequently that the discrepancy between the predictions and measurements of the peak deflections is not associated with the delamination model. Rather, we argue that imperfect clamping of the monolithic beams results in some slippage of the beams at the supports. Thus, the FE calculations that assume perfect clamping under-predict the observed deflections.

5.2.1. Effect of delamination

In order to determine the role of delamination upon the dynamic response of the monolithic beams, two additional sets of FE calculations were conducted:

- no-delamination, where the separate plies of the beams were tied together so as to prevent delamination.
- separate plies, where each ply was decoupled so that the plies could separate and slide relative to each other with no

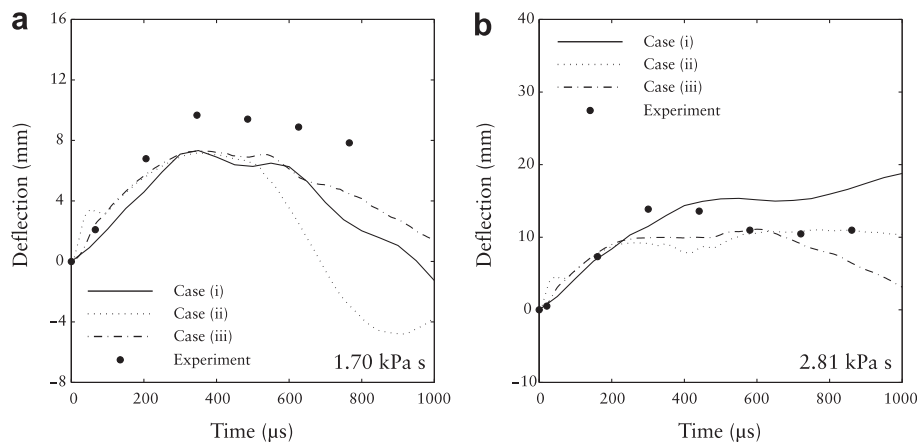


Fig. 16. FE predictions of the temporal variation of the mid-span deflection of the monolithic beam subjected to impulses (a) $I_0 = 1.7$ kPa s and (b) 2.81 kPa s. Calculations are included for three models of the monolithic beams. Case (i): no-delamination, where the separate plies of the beams were tied together; Case (ii) separate plies, where each ply was decoupled and Case (iii) the reference calculation with a cohesive surface modelling delamination between the plies. The corresponding measurements from Fig. 8 are included.

associated traction. Inter-penetration of the plies was prevented via a penalty contact algorithm.

The predicted mid-span deflection versus time histories for these two sets of calculations, along with the measured responses, are shown in Fig. 16a and b for impulse levels $I_0 = 1.7$ kPa s and 2.81 kPa s, respectively. Additionally, the reference solution, wherein a cohesive surface models the delamination between plies, is reported in Fig. 16 and this is referred to as case (iii) in the figure. Intriguingly, the peak deflections for all three predictions are rather similar, and the no-delamination assumption leads to the largest peak deflection at $I_0 = 2.81$ kPa s. In order to rationalise this finding we proceed to investigate the energy absorption due to delamination in the reference calculations.

Consider the case of $I_0 = 2.81$ kPa s. The predicted temporal evolution of the energy absorbed in delamination E_d (summed overall plies) is plotted in Fig. 17 as the ratio E_d/E_0 where E_0 is the initial kinetic energy of the metal foam projectile. The delamination energy initially increases and then attains the steady-state value of $E_d^{ss}/E_0 \approx 0.046$. Thus, delamination absorbs less than 5% of the initial kinetic energy of the projectile with the remainder of the energy existing on the forms of (i) kinetic energy and elastic/plastic deformation of the beam E_{beam} , and (ii) kinetic energy and plastic dissipation within the projectile E_{proj} . The main effect of delamination is to change the mode of deformation of the impacted beams. This is illustrated in Fig. 18a and b where predictions of the deflected shapes of the beams are shown for $I_0 = 1.7$ kPa s and 2.81 kPa s, respectively. Predictions are given at three selected times after impact and for the three cases detailed above, i.e. (i) no delamination; (ii) separate plies and (iii) the reference case. When delamination is permitted in cases (ii) and (iii), the independent motion of the plies results in complex deformation modes while a typical string-like deformation mode is observed in the case (i) of no-delamination.

6. Comparison of the dynamic response of composite and metallic sandwich structures

It is instructive to compare the performance of composite beams subjected to the metal foam impact with metallic equivalents.

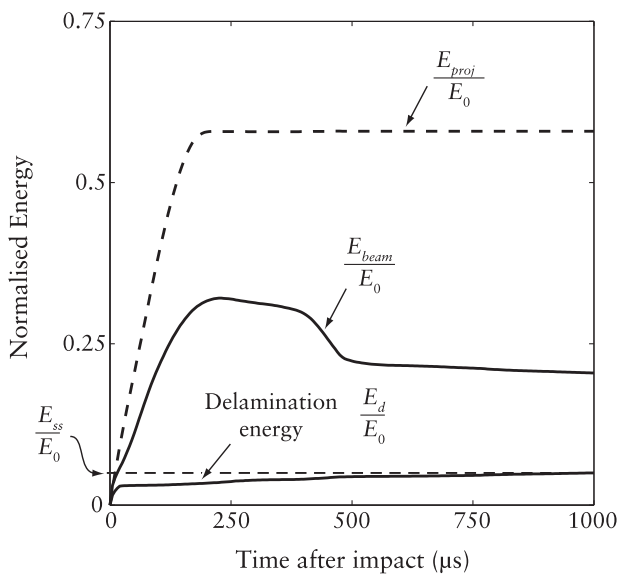


Fig. 17. Predictions (monolithic beam subjected to $I_0 = 2.81$ kPa s) of the temporal variation of the energy absorbed in delamination E_d (summed overall the plies), energy within the beam (E_{beam}) and projectile (E_{proj}). The energies are normalised by the initial kinetic energy E_0 of the metal foam projectile.

Table 3

Geometric parameters of the steel square-honeycomb core sandwich beams used in the investigation by Rathbun et al. [19], and those of the carbon fibre epoxy composite beams. The notation used for the geometric parameters is defined in Fig. 1.

Beam material	l (mm)	b (mm)	H (mm)	L (mm)	t_f (mm)	t_c (mm)	$\bar{\rho}$
Steel	200	32	8.3	12.7	0.64	0.25	0.04
Composite	200	35	14.2	7.1	0.75	0.35	0.1

Ideally, we would wish to compare the performance of square-honeycomb core metallic (e.g. steel) and composite sandwich beams of the same areal mass M and span l . However, given that it is impractical to manufacture square-honeycomb core sandwich beams from steel with an areal mass as low as $M = 5.89$ kg m⁻² we shall compare the performance of the composite beams with stainless steel square-honeycomb sandwich beams as investigated by Rathbun et al. [19]. These clamped steel beams have an areal mass $M = 12.6$ kg m⁻² and the geometric parameters as detailed in Table 3. Although the geometry of the steel and composite sandwich beams are rather different (for example, 20% of the beam mass is in the core of the steel beams, whereas 60% of the beam mass is in the core of the composite beams), the steel and composite beams do possess equal spans of $l = 200$ mm, allowing for their performances to be compared on an equal mass basis using the

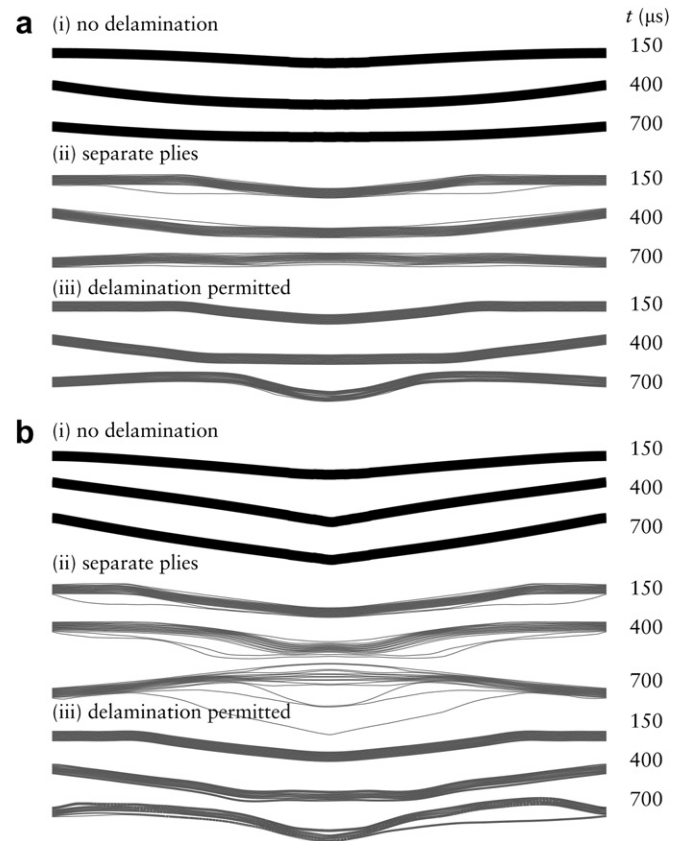


Fig. 18. Predictions of the deflected profiles of the monolithic beams at three selected times t , with $t = 0$ corresponding to the instant of impact. Results are shown for two levels of impulse (a) $I_0 = 1.7$ kPa s and (b) 2.81 kPa s and for three different models of the monolithic beams: Case (i): no-delamination, where the separate plies of the beams were tied together; Case (ii) separate plies, where each ply was decoupled and Case (iii) the reference calculation with a cohesive surface modelling delamination between the plies.

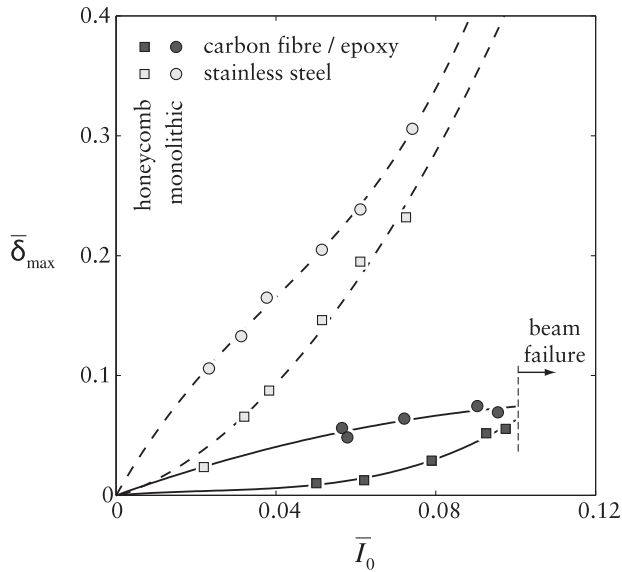


Fig. 19. Comparison between the dynamic performance of steel and composite beams as quantified by the normalised maximum deflections of the back face at mid-span, $\bar{\delta}_{max}$, as a function of the normalised impact impulse \bar{I}_0 . Results for the steel beams are taken from Rathbun et al. [19].

non-dimensional group similar to that suggested by Xue and Hutchinson [29]. Define a non-dimensional impulse

$$\bar{I}_0 = \frac{I_0}{cM} \quad (6.1)$$

where c is a representative wave speed taken here to be $c = 5000 \text{ m s}^{-1}$, that is, the longitudinal elastic wave speed of steel. Also, introduce the non-dimensional peak deflection

$$\bar{\delta}_{max} = \frac{\delta_{max}}{l} \quad (6.2)$$

where δ_{max} is the maximum deflection of the rear face at mid-span. Fig. 19 contains a plot of the measured $\bar{\delta}_{max}$ versus \bar{I}_0 for the steel and composite sandwich beams along with their monolithic counterparts. Note that in calculating \bar{I}_0 we take $M = 5.89 \text{ kg m}^{-2}$ and 12.6 kg m^{-2} for the composite and steel beams respectively. It is evident that:

- Sandwich beams outperform their monolithic counterparts, particularly at low values of \bar{I}_0 for which $\delta_{max} \leq H$. In this bending dominated regime, the higher bending stiffness/strength of the sandwich beams causes them to outperform their monolithic counterparts.
- The composite beams (both monolithic and sandwich) undergo smaller deflections than the steel beams for a given values of \bar{I}_0 suggesting that composite beams outperform steel beams of equal mass on the basis of maximum deflection.
- The monolithic and sandwich beams ruptured at normalised impulses $\bar{I}_0 \geq 0.1$. In contrast, the steel beams survived at the highest levels of impulse investigated by Rathbun et al. [19]. Thus, while composite beams outperform steel beams on the basis of maximum deflections, they undergo catastrophic failure at lower impulses than steel beams of equal mass.

7. Concluding remarks

Metal foam projectiles have been used to impact clamped carbon fibre monolithic and sandwich beams containing a square-

honeycomb core. The dynamic deflections of the beams have been measured as a function of projectile momentum, and the measured responses are compared with finite element (FE) simulations. A range of failure modes were observed in the sandwich beams including core fracture, plug-type shear failure of the core, debonding of the face sheets from the core and tensile fracture of the face sheets at the supports. In the monolithic composite beams only two failure modes were observed: delamination of the plies and tensile failure at the supports.

The constitutive model of Matzenmiller et al. [21] and Hashin [22] for the initiation and development of damage in unidirectional fibre composites, was calibrated against tensile and compressive tests on the carbon fibre composite material sheets. A finite element model was constructed by treating the sandwich beams as an assembly of unidirectional plies, with fibres in the appropriate orientation. Cohesive surfaces between the plies of the face sheets and an adhesive layer between the core and the faces sheets were included in the model in an attempt to predict the delamination and debonding failure modes respectively. When material rate dependence was introduced into the carbon fibre properties, the FE simulations captured the measurements to reasonable fidelity. However, without rate dependence the FE simulation significantly overestimated the deflections. The FE simulations revealed that only a very small fraction of the kinetic energy of the projectile was dissipated by delamination of the plies: the principal effect of delamination is to change the dynamic deformation mode. The dynamic performance of the composite beams has been quantified by the maximum transverse deflection at mid-span as a function of projectile momentum. On this basis, the sandwich beams outperform monolithic composite beams, monolithic steel beams and steel sandwich beams of equal mass. However, the composite beams undergo catastrophic failure at lower impulses than the steel beams of equal mass due to the lower ductility of the composite material.

This study has revealed that the major discrepancies between experiment and predictions are due to the inadequacies of the damage evolution model of the discrepancies between measurement and predictions using the Matzenmiller et al. [21]. Work by Reid and co-workers [30–32] suggest alternative approaches to modelling damage that are suitable to be used in an FE framework. Developing these damage models within an FE setting and examining their fidelity under dynamic loading conditions is suggested as a topic of future work.

Acknowledgements

This work was supported by the Office of Naval Research under ONR grant number N00014-07-1-0764 (Dr David Shifler, Program manager).

References

- [1] Steeves CA, Fleck NA. Collapse mechanisms of sandwich beams with composite faces and a foam core, loaded in three-point bending. Part 1: analytical models and minimum weight design. *International Journal of Mechanical Sciences* 2004;46:561–83.
- [2] Tagarielli VL, Fleck NA, Deshpande VS. Collapse of clamped and simply supported composite sandwich beams in three-point bending. *Composites Part B-Engineering* 2004;35:523–34.
- [3] Zenkert D. An introduction to sandwich construction. London UK: Chameleon Press Ltd; 1996.
- [4] Gibson LJ, Ashby MF. Cellular solids, structure and properties. 2nd ed. Cambridge: Cambridge University Press; 1997.
- [5] Ashby MF, Evans AG, Fleck NA, Gibson LJ, Hutchinson JW, Wadley HN. Metal foams: a design guide. Boston MA: Butterworth-Heinemann; 2000.
- [6] Abrate S. Impact on composite structures. Cambridge University Press; 1998.
- [7] Olsson R. Engineering method for prediction of impact response and damage in sandwich panels. *Journal of Sandwich Structures & Materials* 2002;4:3–29.

- [8] Xu L, Rosakis AJ. Impact failure characteristics in sandwich structures. Part II: effects of impact speed and interfacial strength. *International Journal of Solids and Structures* 2002;39:4237–48.
- [9] Xu L, Rosakis AJ. Impact failure characteristics in sandwich structures Part I: basic failure mode selection. *International Journal of Solids and Structures* 2002;39:4215–35.
- [10] Herup E, Palazotto A. Low-velocity impact damage initiation in graphite/epoxy/Nomex honeycomb-sandwich plates. *Composites Science and Technology* 1998;57:1581–98.
- [11] Mines R. Low velocity perforation behaviour of polymer composite sandwich panels. *International Journal of Impact Engineering* 1998;21:855–79.
- [12] Abrate S. Localized impact on sandwich structures with laminated facings. *Applied Mechanics Reviews* 1997;50:69–82.
- [13] Olsson R, Donadon M, Falzon B. Delamination threshold load for dynamic impact on plates. *International Journal of Solids and Structures* 2006;43:3124–41.
- [14] Moyer ET, Amir GG, Olsson KA, Hellbratt SE. Response of GRP sandwich structures subjected to shock loading. United Kingdom: Engineering Materials Advisory Services Ltd; 1992. p. 49–65.
- [15] Mäkinen K. The transverse response of sandwich panels to an underwater shock wave. *Journal of Fluids and Structures* 1999;13:631–46.
- [16] Tagarielli VL, Deshpande VS, Fleck NA. The dynamic response of composite sandwich beams to transverse impact. *International Journal of Solids and Structures* 2007;44:2442–57.
- [17] Radford DD, Deshpande VS, Fleck NA. The use of metal foam projectiles to simulate shock loading on a structure. *International Journal of Impact Engineering* 2005;31:1152–71.
- [18] Radford D, Fleck NA, Deshpande VS. The response of clamped sandwich beams subjected to shock loading. *International Journal of Impact Engineering* 2006;32:968–87.
- [19] Rathbun HJ, Radford DD, Xue Z, He MY, Yang J, Deshpande V, et al. Performance of metallic honeycomb-core sandwich beams under shock loading. *International Journal of Solids and Structures* 2006;43:1746–63.
- [20] Russell BP, Liu T, Fleck NA, Deshpande VS. Quasi-static three-point bending of carbon fibre sandwich beams with square-honeycomb cores, *ASME Journal of Applied Mechanics*, in press.
- [21] Matzenmiller A, Lubliner J, Taylor RL. A constitutive model for anisotropic damage in fiber-composites. *Mechanics of Materials* 1995;20:125–52.
- [22] Hashin Z. Failure criteria for unidirectional fiber composites. *ASME Journal of Applied Mechanics* 1980;47:329–34.
- [23] Russell BP, Deshpande VS, Wadley HNG. Quasi-static deformation and failure modes of composite square-honeycombs. *Journal of Mechanics of Materials and Structures* 2008;3:1315–40.
- [24] Radford DD, McShane GJ, Deshpande VS, Fleck NA. The response of clamped sandwich plates with metallic foam cores to simulated blast loading. *International Journal of Solids and Structures* 2006;43:2243–59.
- [25] McShane GJ, Radford DD, Deshpande VS, Fleck NA. The response of clamped sandwich plates with lattice cores subjected to shock loading. *European Journal of Mechanics - A/Solids* 2006;25:215–29.
- [26] Redux 319 Film Adhesive neat resin data sheet, Hexcel Composites, Duxford, UK.
- [27] Deshpande VS, Fleck NA. High strain rate compressive behaviour of aluminium alloy foams. *International Journal of Impact Engineering* 2000;24:277–98.
- [28] Deshpande VS, Fleck NA. Isotropic constitutive models for metallic foams. *Journal of the Mechanics and Physics of Solids* 2000;48:1253–83.
- [29] Xue ZY, Hutchinson JW. A comparative study of impulse-resistant metal sandwich plates. *International Journal of Impact Engineering* 2004;30:1283–305.
- [30] Li S, Reid SR, Soden PD. A continuum damage model for transverse matrix cracking in laminated fibre-reinforced composites. *Philosophical Transactions of the Royal Society, London* 1998;A356:2379–412.
- [31] Zou Z, Reid SR, Li S. A continuum damage model for delamination in laminated composites. *Journal of the Mechanics and Physics of Solids* 2003;51:333–56.
- [32] Li S, Reid SR, Soden PD, Hinton MJ. Modelling transverse cracking damage in thin, filament-wound tubes subjected to lateral indentation followed by internal pressure. *International Journal of Mechanical Sciences* 2005;47:621–46.